Commun Nonlinear Sci Numer Simulat 95 (2021) 105658

Contents lists available at ScienceDirect

Commun Nonlinear Sci Numer Simulat

journal homepage: www.elsevier.com/locate/cnsns

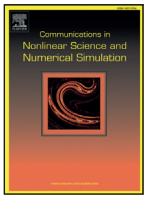

Research paper

An unconditionally stable scheme for the Allen–Cahn equation with high-order polynomial free energy

Chaeyoung Lee[a], Hyundong Kim[a], Sungha Yoon[a], Sangkwon Kim[a], Dongsun Lee[b], Jinate Park[a], Soobin Kwak[a], Junxiang Yang[a], Jian Wang[c], Junseok Kim[a,*]

[a] Department of Mathematics, Korea University, Seoul 02841, Republic of Korea
[b] Department of Mathematics Education, Incheon National University, Incheon 21999, Republic of Korea
[c] School of Mathematics and Statistics, Nanjing University of Information Science and Technology, Nanjing, 210044, China

ARTICLE INFO

Article history:
Received 20 June 2020
Revised 1 December 2020
Accepted 3 December 2020
Available online 5 December 2020

Keywords:
Allen–Cahn equation
Polynomial free energy
Operator splitting method

ABSTRACT

In this paper, we propose an unconditionally stable numerical scheme for the Allen–Cahn (AC) equation with high-order (higher than fourth) polynomial free energy. The AC equation was proposed by Allen and Cahn to model the anti-phase domain coarsening in a binary mixture. The AC equation has been extensively used as a building block equation for modeling many scientific problems such as image processing, dendritic growth, motion by mean curvature, and multi-phase fluid flows. The AC equation can be derived from a gradient flow of a total energy functional which consists of a double-well form potential and a gradient term. Practically, a quartic polynomial has been used for the double-well potential. High-order (greater than fourth) polynomial free energy potentials can be also used in the total energy functional and can better represent interfacial dynamics of the AC equation. However, the AC equation with the high-order polynomial is getting stiffer as the polynomial order increases. Typically, this type of double-well potential is solved using a convex splitting with a stabilizing parameter and effectively modifies the original governing equation.

In the proposed method, we use a second-order operator splitting method and an interpolation method. First, we solve the nonlinear double-well potential term using interpolation from the pre-computed values. Second, we solve the diffusion equation using the Crank–Nicolson method and multigrid method. The overall scheme is unconditionally stable and we theoretically prove the unconditional stability. Computational experiments are performed to demonstrate the robustness and accuracy of the proposed method; and investigate the effect of the order of the double-well potential on the dynamics of the AC equation. Finally, we highlight the different dynamics for the AC equation with polynomial free energy of various orders. The computational results suggest that the proposed method will be useful for modeling various interfacial phenomena.

* Corresponding author.
E-mail address: cfdkim@korea.ac.kr (J. Kim).

https://doi.org/10.1016/j.cnsns.2020.105658
1007-5704/

1. Introduction

The Allen–Cahn (AC) equation was presented by Allen and Cahn [1]:

$$\frac{\partial \phi(\mathbf{x},t)}{\partial t} = -\frac{F'(\phi(\mathbf{x},t))}{\epsilon^2} + \Delta\phi(\mathbf{x},t), \quad \mathbf{x}\in\Omega, t>0, \tag{1}$$

where $\phi(\mathbf{x},t)$ is the order parameter in a domain $\Omega\subset\mathbb{R}^d$ $(d=2,3)$, $F(\phi)$ is the double-well free energy density, and ϵ is a positive parameter. For the boundary condition in this work, a homogeneous Neumann boundary condition is considered. The AC equation can be obtained from the following Lyapunov energy functional in L^2-gradient flow:

$$\mathcal{E}(\phi) = \int_\Omega \left(\frac{F(\phi)}{\epsilon^2} + \frac{|\nabla\phi|^2}{2}\right)\mathrm{d}\mathbf{x}. \tag{2}$$

Differentiating Eq. (2) with respect to time gives the following total energy decrease in time:

$$\begin{aligned}\frac{\mathrm{d}}{\mathrm{d}t}\mathcal{E}(\phi) &= \int_\Omega \left(\frac{\partial\phi}{\partial t}\frac{F'(\phi)}{\epsilon^2} + \nabla\frac{\partial\phi}{\partial t}\cdot\nabla\phi\right)\mathrm{d}\mathbf{x}\\ &= \int_\Omega \phi_t\left(\frac{F'(\phi)}{\epsilon^2} - \Delta\phi\right)\mathrm{d}\mathbf{x} = -\int_\Omega (\phi_t)^2\mathrm{d}\mathbf{x} \le 0.\end{aligned} \tag{3}$$

The AC equation has been extensively used as a building block equation for modeling many important scientific problems such as image processing [2], dendritic growth [3,4], motion by mean curvature [5], the evaporation of thin film mixtures [6], and multi-phase fluid flows [7–9]. In addition, the AC equation has been modified in other forms and utilized in many areas. For example, many studies have been conducted on the conservative AC equation [10,11] because of the nature of preserving mass unlike classical AC equation. Recently, pinning boundary conditions have been applied to the AC equation and the conservative AC equation [12].

Therefore, the accurate and efficient numerical schemes are needed to solve the AC equation. The efficient and robust numerical method in [13] was based on the diagonally implicit fractional-step θ-scheme for temporal discretization and the conforming finite element method (FEM) for spatial discretization. The authors in [14] designed, analyzed, validated an unconditionally energy stable second-order FEM for solving the AC equation. Shen et al. [15] investigated a class of the maximum principle preserving schemes for the generalized AC equation. In [16], a linearized finite difference method (FDM) for solving the AC equation was proposed using a modified leap-frog scheme and they rigorously analyzed a maximum norm error to show that the proposed scheme is second-order accurate both in time and space variables. The analysis of the operator splitting schemes for the numerical solution of the AC equation was studied [17,18]. Tianliang et al. [19] developed a novel second-order maximum-principle preserving FDM for the AC equation and demonstrated that the method is unconditionally energy-stable. The authors in [20] proposed a volume-preserving time-fractional AC equation and adaptive linear second-order energy stable schemes. They showed the efficiency and advantages of the presented scheme through numerical results. Other than the operator splitting approach, there have been extensive works of second-order accurate energy stable numerical schemes for the phase-field model [21] and other related gradient flows, using the implicit treatment for the nonlinear terms. Cheng et al. [22] presented an energy gradient stable numerical scheme for the Cahn–Hilliard (CH) equation with the second-order accuracy in time and fourth-order finite difference scheme in space. A modified backward differentiation formula (BDF2) is applied for the temporal accuracy. Wu et al. [23] used the standard Crank–Nicolson method to handle the high-order linear diffusion term. In [24], the second-order convex splitting scheme was used with the Fourier pseudo-spectral spatial approximation. In addition, there has been recent work of energy stable numerical schemes for ternary CH system, one of popular phase-field models, in which a high order polynomial of mixed terms was involved, using convex splitting techniques [25].

The main purpose of this paper is to propose an unconditionally stable numerical scheme and investigate the dynamics of the AC equation with the high-order (higher than fourth) polynomial free energy:

$$F_\alpha(\phi) = 0.25(\phi^\alpha - 1)^2, \tag{4}$$

where α is an even integer, see Fig. 1. Note that if $\alpha = 2$, then $F_\alpha(\phi)$ becomes the classical quartic polynomial potential.

In general, phase-field models such as the AC equation replace a sharp interface by a diffuse phase transition layer with a finite thickness. To numerically solve the AC equation with a small interfacial transition parameter, we need a sufficiently fine mesh size to discretize phase interfaces [26]. The main motivation for using higher-order polynomial ($\alpha > 2$) is that we can use relatively coarser mesh sizes to resolve the phase interfaces. To demonstrate the performance of the proposed model, we perform various computational tests in the numerical experiment section.

To the authors' knowledge, there are only few studies on the AC equation with a high-order polynomial free energy potential. Recently, a high-order polynomial potential was used in the Navier–Stokes–Cahn–Hilliard systems for the two-phase incompressible fluids [27]:

$$\mathbf{u_t} + \mathbf{u}\cdot\nabla\mathbf{u} = -\nabla p + \frac{1}{Re}\Delta\mathbf{u} - \frac{1}{2We}\nabla\cdot\left(\frac{\nabla\phi}{|\nabla\phi|}\right)\nabla\phi, \tag{5}$$

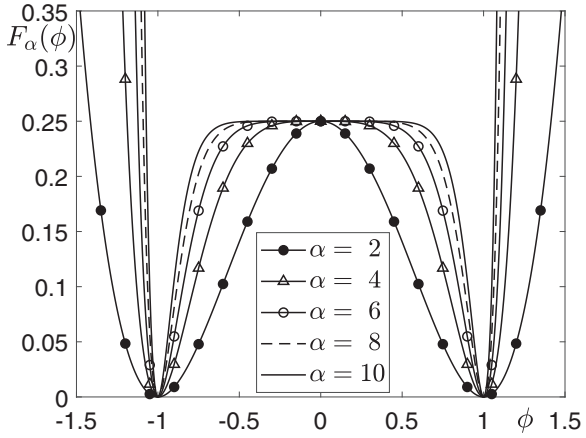

Fig. 1. Polynomial free energy functions, $F_\alpha(\phi) = 0.25(\phi^\alpha - 1)^2$, for $\alpha = 2, 4, 6, 8$, and 10.

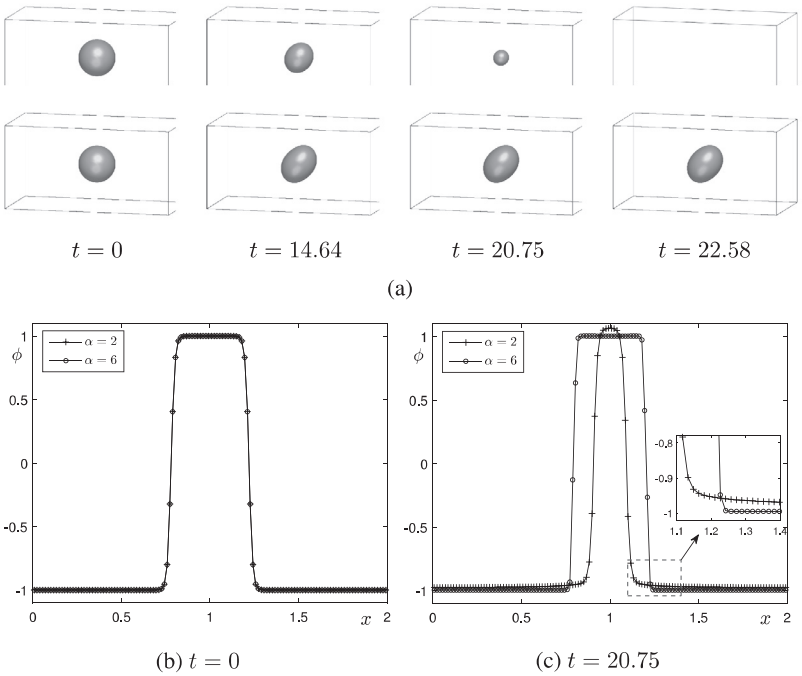

Fig. 2. (a) Temporal evolutions of droplet under a simple shear flow with $\alpha = 2$ (top row) and $\alpha = 6$ (bottom row). (b)–(c) Profiles of ϕ sliced in $y - z$ plane through $x = 0$ at $t = 0$ and $t = 20.75$, respectively.

$$\nabla \cdot \mathbf{u} = 0, \tag{6}$$

$$\phi_t + \nabla \cdot (\phi \mathbf{u}) = \frac{1}{Pe} \Delta (F'_\alpha(\phi) - \epsilon^2 \Delta \phi), \tag{7}$$

where $\mathbf{u} = (u, v, w)$ is the velocity and p is the pressure. For the other parameters, please refer to [27]. The initial radius of sphere is 0.22 in the computational domain $\Omega = (0, 2) \times (0, 1) \times (0, 1)$ with $128 \times 64 \times 64$ mesh. Fig. 2(a) shows the droplet deformation under shear flow with $\alpha = 2$ (top row) and $\alpha = 6$ (bottom row) in three-dimensional space. The droplet with $\alpha = 2$ is vanishing as time evolves although the governing system (5)–(7) should satisfy the mass conservation property. To prevent this problem, the mesh grid size must be small enough, however, its computational cost is very expensive, in particular, for three-dimensional space. It is known that when the mesh grid size is $h = 1/64$ in three-dimensional space and the initial radius smaller than $19h = 0.296875$, the spherical shape is unstable and diffuses into the ambient bulk phase to

decrease its total energy [28]. On the other hand, the droplet with $\alpha = 6$ does not shrink even if the mesh grid size is used as the same with the case with $\alpha = 2$. When the high-order polynomial potential is used, the spherical drop needs relatively small number grids to preserve its shape [27]. Fig. 2(b) and (c) show x-directional profiles of ϕ through $(y, z) = (0.5, 0.5)$ at $t = 0$ and $t = 20.75$, respectively. Therefore, the high-order polynomial potential has good property to conserve features compared to the fourth-order polynomial potential.

The remaining parts of this paper are organized as follows. Section 2 describes the numerical solution algorithm for the AC equation with the high-order polynomial potential. Numerical experiments to show the effects and differences of using high-order α are described in Section 3. Finally, Section 4 discusses the conclusions.

2. Numerical solution algorithm

In this section, we present an unconditionally stable numerical solution algorithm of the AC equation with the high-order polynomial free energy. First, we discretize the AC equation in two-dimensional space $\Omega = (L_x, R_x) \times (L_y, R_y)$. For positive even integers N_x and N_y, the uniform spatial step size in the x-and y-directions is denoted by $h = (R_x - L_x)/N_x = (R_y - L_y)/N_y$. The numerical solution $\phi(x_m, y_n, t_k)$ can be simply denoted by ϕ^k_{mn}, where $(x_m, y_n) = (L_x + (m - 0.5)h,\ L_y + (n - 0.5)h)$ is cell-centered point, $t_k = k\Delta t$, and Δt is the temporal step size. The three-dimensional numerical solution algorithms can be defined similarly.

For the second-order operator splitting method, we need three substeps as follows [29]:

$$\phi(\mathbf{x}, t + \Delta t) = \left(\mathcal{N}^{\Delta t/2} \circ \mathcal{L}^{\Delta t} \circ \mathcal{N}^{\Delta t/2}\right)\phi(\mathbf{x}, t) + \mathcal{O}(\Delta t^3),\ \ \mathbf{x} \in \Omega, t > 0, \tag{8}$$

where $\mathcal{N}^{\Delta t}$ and $\mathcal{L}^{\Delta t}$ are the nonlinear and linear solution operators with the temporal step Δt, respectively. The nonlinear solution operator is $\mathcal{N}^{\Delta t}\phi(\mathbf{x}, t) = \phi(\mathbf{x}, t + \Delta t)$, where $\phi(\mathbf{x}, t + \Delta t)$ is the solution of the nonlinear differential equation $\phi_t = -F'_\alpha(\phi)/\epsilon^2$ after time Δt with an initial condition $\phi(\mathbf{x}, t)$. The linear solution operator is $\mathcal{L}^{\Delta t}\phi(\mathbf{x}, t) = \phi(\mathbf{x}, t + \Delta t)$, where $\phi(\mathbf{x}, t + \Delta t)$ is the solution of the linear differential equation $\phi_t = \Delta\phi$ after time Δt with an initial condition $\phi(\mathbf{x}, t)$. When both the operators of Eq. (8) have at least second-order accuracy in time, the entire numerical method theoretically guarantees second-order accuracy in time [29–31]. There have been theoretical analysis of convergence estimate for various nonlinear partial differential equations [25,32].

In the proposed method, we use an interpolation method to solve the nonlinear equation ($\phi_t = -F'_\alpha(\phi)/\epsilon^2$) and the Crank–Nicolson method with a multigrid method to solve the linear equation ($\phi_t = \Delta\phi$). We describe each of these numerical solution algorithms in detail. First, we condition the nonlinear equation:

$$\frac{\partial\phi(\mathbf{x}, t)}{\partial t} = -\frac{F'_\alpha(\phi(\mathbf{x}, t))}{\epsilon^2} \tag{9}$$

with the initial condition $\phi(x_m, y_n, k\Delta t)$. Note that if $\alpha = 2$, then we have a closed-form solution [33],

$$\phi(x_m, y_n, (k+1)\Delta t) = \phi^k_{mn} \Big/ \sqrt{e^{-\frac{2\Delta t}{\epsilon^2}} + \left(\phi^k_{mn}\right)^2\left(1 - e^{-\frac{2\Delta t}{\epsilon^2}}\right)}. \tag{10}$$

However, if $\alpha \neq 2$, then a simple closed-form solution is not available. We have to resort to numerical solutions. When the value of α is large, we cannot use both the explicit and implicit methods because the equation is very stiff and time step restriction is extremely stringent. The large values of α can lead to rapid oscillations in the solution of Eq. (9) even with moderate time steps.

For concrete examples, first let us consider the explicit method for Eq. (9):

$$\frac{\phi^{k+1} - \phi^k}{\Delta t} = -\frac{F'_\alpha(\phi^k)}{\epsilon^2}. \tag{11}$$

The initial condition is $\phi^0 = 0.95$; and we set $\alpha = 20$ and $\epsilon = 1$. Fig. 3(a) shows the numerical solutions of Eq. (11) with different temporal step sizes ($\Delta t = 0.005,\ 0.01,\ 0.015$). If we use a slightly large temporal step size ($\Delta t = 0.015$), then the solution oscillates. The solution should monotonically increase or decrease with time. Next, we solve Eq. (9) using the implicit method:

$$\frac{\phi^{k+1} - \phi^k}{\Delta t} = -\frac{F'_\alpha(\phi^{k+1})}{\epsilon^2}. \tag{12}$$

We define $G(\phi) = (\phi - \phi^k)/\Delta t + F'_\alpha(\phi)/\epsilon^2$, and then we solve $G(\phi^{k+1}) = 0$ using the Newton's method:

$$\phi^{k+1,p+1} = \phi^{k+1,p} - \frac{G(\phi^{k+1,p})}{G'(\phi^{k+1,p})},\ \text{ for } p = 0, 1, \ldots,$$

where $\phi^{k+1,0} = \phi^k$. We define $\phi^{k+1} = \phi^{k+1,p+1}$ for some p if $|\phi^{k+1,p+1} - \phi^{k+1,p}| < tol$ is satisfied with a given tolerance tol. However, Fig. 3(b) shows that the numerical solution does not converge with a temporal step size $\Delta t = 0.055$. Therefore, the numerical solutions of both the explicit and implicit methods are unstable unless the temporal step size is taken to be sufficiently small.

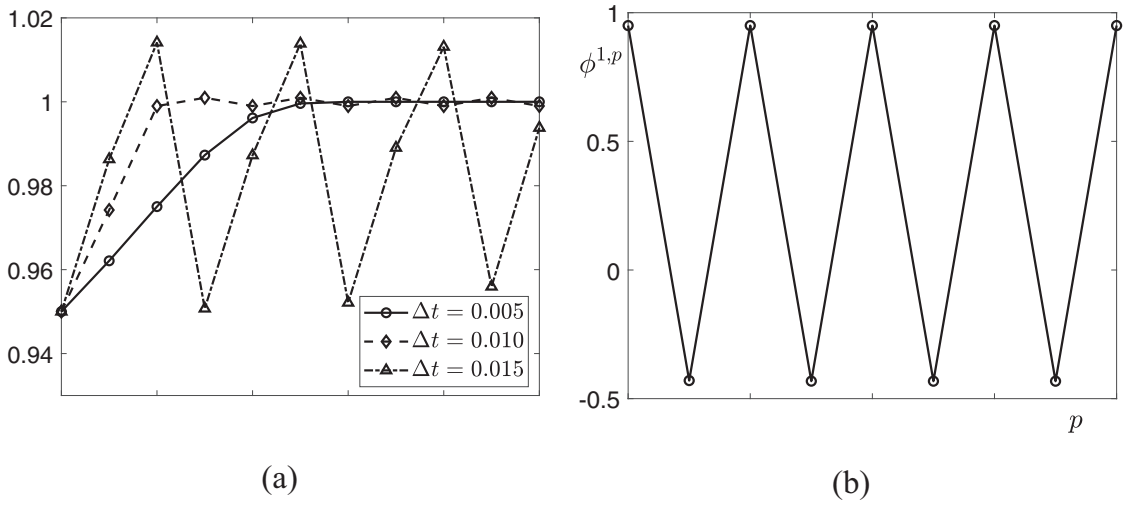

Fig. 3. Numerical results with (a) explicit and (b) implicit Euler methods.

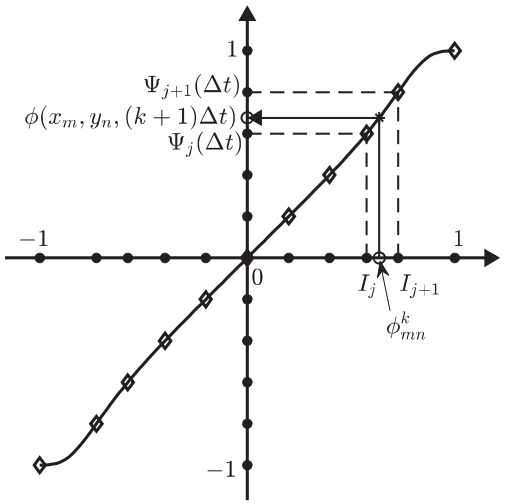

Fig. 4. Schematic diagram of the interpolation step.

To overcome these difficulties, a simple interpolation-based numerical scheme is proposed. The main procedure of the proposed algorithm is as follows: Given ϕ^k_{mn}, we apply the interpolation method with the pre-computed values in order to obtain the solution $\phi(x_m, y_n, (k+1)\Delta t)$. The pre-computed values are the solutions of the nonlinear Eq. (9) using a numerical scheme that will be covered after this paragraph. For example, there is a node I_j satisfying $I_j \le \phi^k_{mn} \le I_{j+1}$ for some j and $1 \le j \le M_2 - 1$. Here, I is a non-uniform grid on the horizontal interval $[-1, 1]$, I_j is an element of I, and M_2 is an odd integer. Then, we define

$$\phi(x_m, y_n, (k+1)\Delta t) = \frac{I_{j+1} - \phi^k_{mn}}{I_{j+1} - I_j}\Psi_j(\Delta t) + \frac{\phi^k_{mn} - I_j}{I_{j+1} - I_j}\Psi_{j+1}(\Delta t). \tag{13}$$

Fig. 4 illustrates the interpolation step using the pre-computed solutions of two adjacent data points of given ϕ^k_{mn}.

A detailed explanation of the proposed algorithm for solving Eq. (9) is given as follows: Given α, ϵ, and temporal step Δt, let us introduce a smaller subcycling time step $\Delta\tau = \Delta t/N_\tau$, where N_τ is a positive integer and its specific value will be defined later. We temporally discretize horizontal interval $[-1,\ 1]$ of possible range of ϕ uniformly, i.e., $I^* = \{I^*_i | I^*_i = -1 + 2(i-1)/(M_1 - 1),\ \text{for } i = 1, \ldots, M_1\}$. Here, M_1 is an odd integer to include zero in I^*. Fig. 5(a) shows the numerical solutions of the ordinary differential Eq. (9) on I^* and at $t = \Delta t$ by using the explicit Euler scheme with the subcycling time step $\Delta\tau$ and the initial condition, $\Psi_i(0) = I^*_i$. That is, for $i = 1, \ldots, M_1$,

$$\Psi_i((s+1)\Delta\tau) = \Psi_i(s\Delta\tau) - \Delta\tau\frac{F'_\alpha(\Psi_i(s\Delta\tau))}{\epsilon^2},\ \text{for } s = 0, \ldots, N_\tau - 1. \tag{14}$$

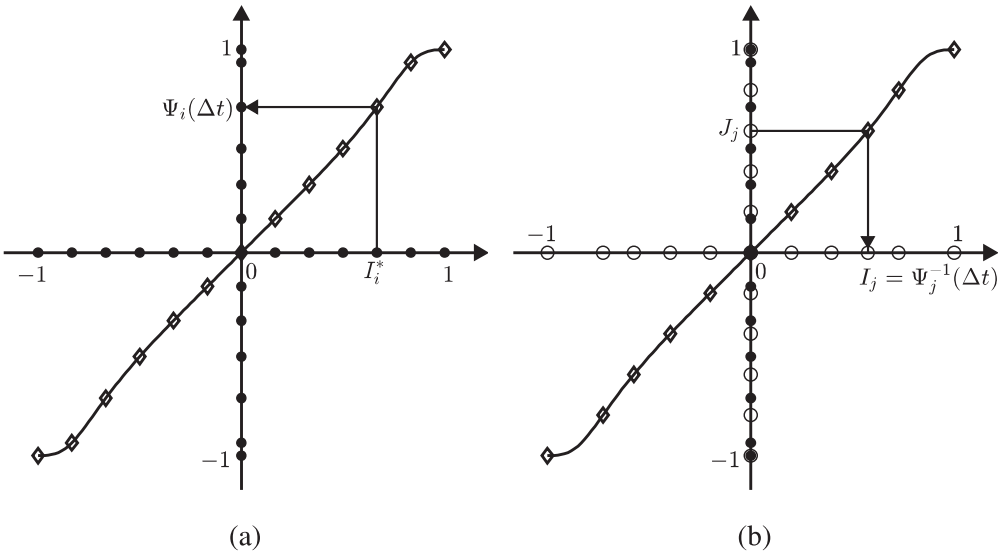

Fig. 5. Schematic diagrams. (a) The numerical solutions $\Psi(\Delta t)$ of Eq. (9) on the uniform grid I^*. (b) The inverse mapping $\Psi^{-1}(\Delta t)$ on the uniform grid J.

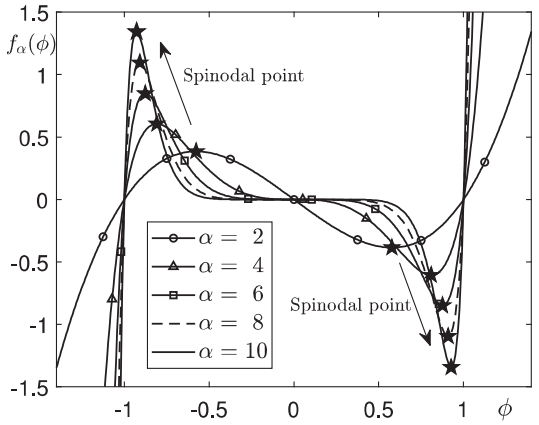

Fig. 6. First-order derivatives of $F_\alpha(\phi)$, $f_\alpha(\phi) = F'_\alpha(\phi) = 0.5\alpha(\phi^\alpha - 1)\phi^{\alpha-1}$ for $\alpha = 2, 4, 6, 8$, and 10. The symbiotic stars in the upper left and lower right corners indicate spinodal points. The absolute value $|\phi|$ of spinodal point reaches the value 1 as α increases.

Next, we discretize the vertical interval $[-1,\ 1]$ uniformly, i.e., $J = \{J_j | J_j = -1 + 2(j-1)/(M_2 - 1),\ \text{for } j = 1, \ldots, M_2\}$. Here, M_2 is an odd integer to include zero in J. Using interpolation and inverse mapping, we redefine a non-uniform grid on the horizontal interval $[-1,\ 1]$, i.e., $I = \{I_j | I_j = \Psi_j^{-1}(\Delta t),\ \text{for } j = 1, \ldots, M_2\}$ as shown in Fig. 5(b). On this non-uniform grid I, we solve the ordinary differential Eq. (9) by using the explicit Euler scheme with the subcycling time step $\Delta\tau$ and the initial condition, $\Psi_j(0) = I_j$. That is, for $j = 1, \ldots, M_2$,

$$\Psi_j((s+1)\Delta\tau) = \Psi_j(s\Delta\tau) - \Delta\tau \frac{F'_\alpha(\Psi_j(s\Delta\tau))}{\epsilon^2},\ \text{for } s = 0, \ldots, N_\tau - 1. \tag{15}$$

Finally, we keep the non-uniform grid I and the numerical solutions $\Psi_j(\Delta t)$ for $I_j \in I,\ j = 1, \ldots, M_2$ for later use.

Now, we consider the appropriate value of $\Delta\tau$ to stably integrate Eq. (9) for the given α, ϵ, and temporal step Δt. If $I_j = -1, 0$, or 1, then from Eq. (14) we have

$$\Psi_j((s+1)\Delta\tau) = I_j,\ \text{for } s = 0, \ldots, N_\tau - 1. \tag{16}$$

Next, let us assume $0 < I_j < 1$ and $\Psi_j(0) = I_j$, then from Eq. (14) we have

$$\Psi_j(\Delta\tau) = I_j - \Delta\tau \frac{F'_\alpha(I_j)}{\epsilon^2}. \tag{17}$$

As shown in Fig. 6, $F'_\alpha(I_j) = 0.5\alpha(I_j^\alpha - 1)I_j^{\alpha-1} < 0$ for $0 < I_j < 1$, therefore, we have $\Psi_j(\Delta\tau) > 0$ from Eq. (17).

We want to bound $\Psi_j(\Delta\tau)$ by one. That is, $I_j - \Delta\tau F'_\alpha(I_j)/\epsilon^2 < 1$ and $\Delta\tau$ should satisfy $\Delta\tau < \epsilon^2(I_j - 1)/F'_\alpha(I_j)$. Because $\epsilon^2(I_j - 1)/F'_\alpha(I_j)$ is decreasing with respect to I_j on the interval $0 < I_j < 1$, we compute the limit of $\epsilon^2(I_j - 1)/F'_\alpha(I_j)$ as I_j

approaches one, that is,

$$\Delta\tau \le \lim_{I_j\to 1}\frac{\epsilon^2(I_j-1)}{F'_\alpha(I_j)} = \lim_{I_j\to 1}\frac{\epsilon^2}{F''_\alpha(I_j)} = \frac{2\epsilon^2}{\alpha^2}, \tag{18}$$

where we have used L'Hôpital's Rule. Similarly, if $-1 < I_j < 0$, then we have the same condition to Eq. (18). Therefore, we showed that if $|I_j| \le 1$ and $\Delta\tau < 2\epsilon^2/\alpha^2$, then we have

$$|\Psi_j((s+1)\Delta\tau)| \le 1, \text{ for } s = 0,\dots,N_\tau - 1. \tag{19}$$

The condition $\Delta\tau < 2\epsilon^2/\alpha^2$ implies $N_\tau > \alpha^2\Delta t/(2\epsilon^2)$. We set $N_\tau = [\alpha^2\Delta t/(2\epsilon^2)] + 1$ unless otherwise specified. Here, $[x]$ is the greatest integer less than or equal to x. Note that, for accurate computation, we can use a large value of N_τ.

Next, we solve the following linear equation by the Crank–Nicolson finite difference method [34]:

$$\frac{\partial\phi(\mathbf{x},t)}{\partial t} = \Delta\phi(\mathbf{x},t). \tag{20}$$

We discretize Eq. (20) using the Crank–Nicolson method:

$$\frac{\phi^{k+1}_{mn} - \phi^k_{mn}}{\Delta t} = \frac{1}{2}\left(\Delta_h\phi^k_{mn} + \Delta_h\phi^{k+1}_{mn}\right), \tag{21}$$

where the discrete Laplacian operator $\Delta_h\phi^k_{mn} = (\phi^k_{m+1,n} + \phi^k_{m-1,n} + \phi^k_{m,n+1} + \phi^k_{m,n-1} - 4\phi^k_{mn})/h^2$, and solve Eq. (21) using the linear multigrid method [35]. It is well known that the Crank–Nicolson method applied to the heat equation with central finite differences in space is unconditionally stable using the von Neumann stability analysis [34]. Therefore, the overall numerical solution algorithms are unconditionally stable because both the nonlinear and linear solution operators are unconditionally stable. We note that the proposed scheme also satisfies the maximum principle: if $\|\phi^k\|_\infty \le 1$ for any k, then $\|\phi^{k+1}\|_\infty \le 1$, which is easily derived from the boundedness of the solution operators.

3. Numerical experiments

In this section, we perform various computational experiments such as total energy dissipation, stability, accuracy, motion by mean curvature, effects of the model and numerical parameters to demonstrate the accuracy and efficiency of the proposed method. Unless otherwise specified, we use $M_1 = M_2 = 101$ and $N_\tau = 4$. In the multigrid method, two Gauss–Seidel iterations are used for the relaxation steps with a tolerance, $1.0E-7$.

3.1. Energy dissipation

First, we examine the energy dissipation over time with respect to each order $\alpha = 2,\ 4,\ 6,\ 8,$ and 10. The two-dimensional discrete energy $\mathcal{E}(\phi^k)$ is calculated as follows:

$$\mathcal{E}(\phi^k) = \sum_{m=1}^{N_x}\sum_{n=1}^{N_y}\frac{F(\phi^k_{mn})}{\epsilon^2}h^2 + \sum_{m=1}^{N_x-1}\sum_{n=1}^{N_y-1}\frac{(\phi^k_{m+1,n}-\phi^k_{mn})^2 + (\phi^k_{m,n+1}-\phi^k_{mn})^2}{2}. \tag{22}$$

A simple extension to the three-dimensional space yields the following discrete energy,

$$\begin{aligned}\mathcal{E}(\phi^k) = &\sum_{m=1}^{N_x}\sum_{n=1}^{N_y}\sum_{o=1}^{N_z}\frac{F(\phi^k_{mno})}{\epsilon^2}h^3 \\ &+h\sum_{m=1}^{N_x-1}\sum_{n=1}^{N_y-1}\sum_{o=1}^{N_z-1}\frac{(\phi^k_{m+1,no}-\phi^k_{mno})^2 + (\phi^k_{m,n+1,o}-\phi^k_{mno})^2 + (\phi^k_{mn,o+1}-\phi^k_{mno})^2}{2}.\end{aligned} \tag{23}$$

Fig. 7 shows the non-dimensional discrete total energy dissipation in the two- and three-dimensional space, respectively, over time up to various orders $\alpha = 2,\ 4,\ 6,\ 8,$ and 10. The computational domain is given as $\Omega = (-1.2, 1.2)\times(-1.2, 1.2)$ and the final time is set to $t = 0.4$ for the two-dimensional case; similar settings are given, $\Omega = (-1.2, 1.2)\times(-1.2, 1.2)\times(-1.2, 1.2)$ and $t = 0.2$ for the three-dimensional case. The parameter values used are $N_x = N_y = N_z = 128$, $h = 2.4/128$, $\Delta t = 1.0E-4$, and $\epsilon = 0.05$. Here, the initial conditions are set to be $\phi^0_{mn} = 1$ if $(x_m, y_n) \in (20h, 108h)\times(20h, 108h)$; otherwise $\phi^0_{mn} = -1$ and $\phi^0_{mno} = 1$ if $(x_m, y_n, z_o) \in (20h, 108h)\times(20h, 108h)\times(20h, 108h)$; otherwise $\phi^0_{mno} = -1$ in the two- and three-dimensional space, respectively. Note that the energy is normalized by $\mathcal{E}(\phi^1)$ to fix the starting value as 1.

3.2. Stability of the proposed scheme

We demonstrate the unconditional stability of the proposed scheme with a numerical simulation of phase separation in a binary mixture. The initial condition is given as random perturbation with the maximum amplitude 0.5 on the computational domain $\Omega = (-1.2, 1.2)\times(-1.2, 1.2)$:

$$\phi(x, y, 0) = 0.5\text{rand}(x, y), \tag{24}$$

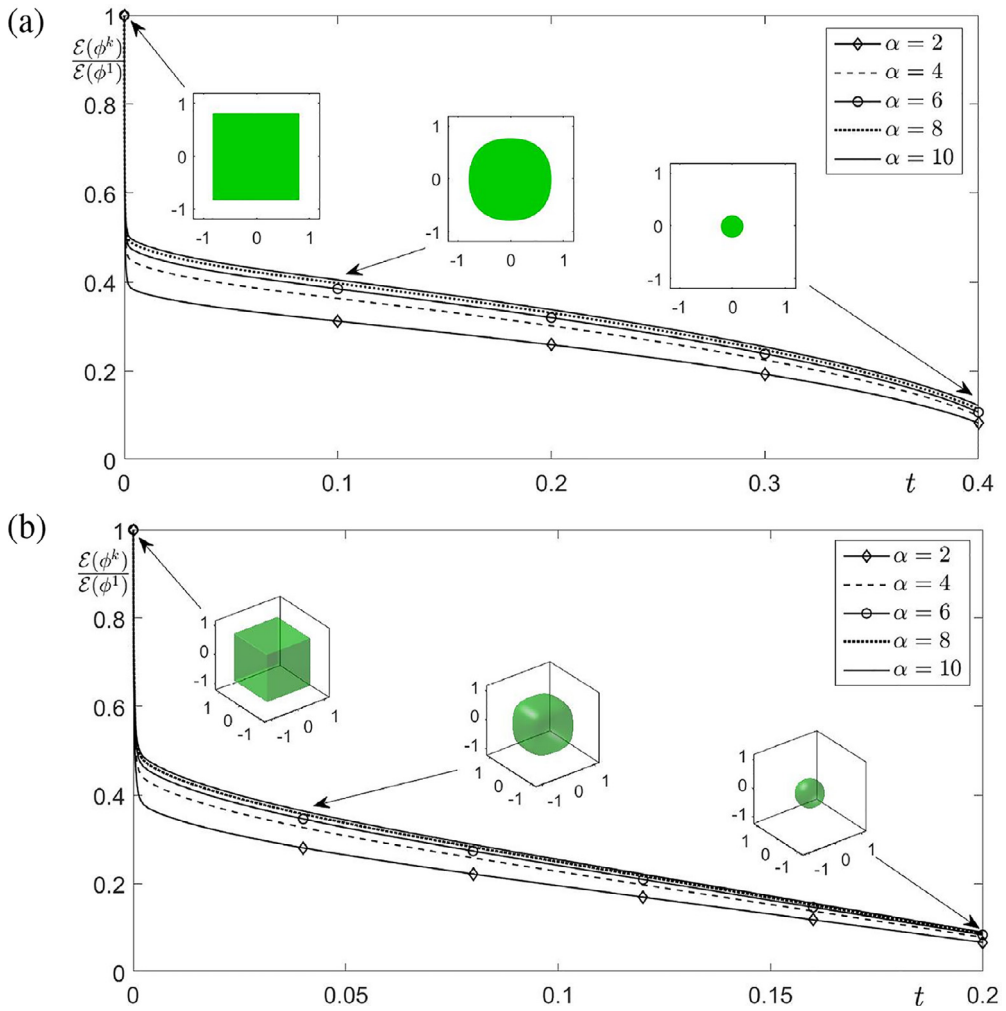

Fig. 7. Dissipation of non-dimensional discrete total energy $\mathcal{E}(\phi^k)/\mathcal{E}(\phi^1)$ with various orders over time in the (a) two- and (b) three-dimensional space, respectively.

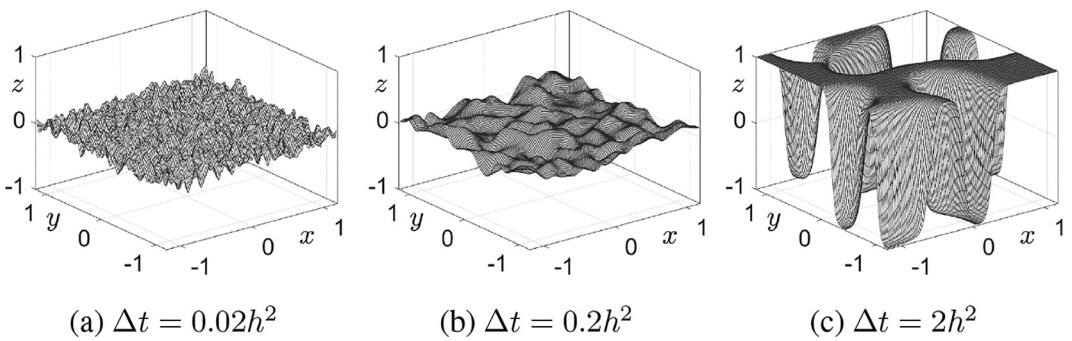

Fig. 8. Snapshots after 50 time step iterations with three different temporal step sizes.

where rand(x, y) is a random value uniformly distributed between -1 and 1. We use the following parameters: $\alpha = 2$, $N_x = N_y = 128$, $h = 2.4/128$, and $\epsilon = 0.05$. Fig. 8(a)–(c) illustrate the snapshots at 50 time step iterations with different temporal steps $\Delta t = 0.02h^2$, $0.2h^2$, and $2h^2$, respectively. The numerical solutions do not blow up when large temporal step sizes are used, therefore, the scheme is unconditionally stable.

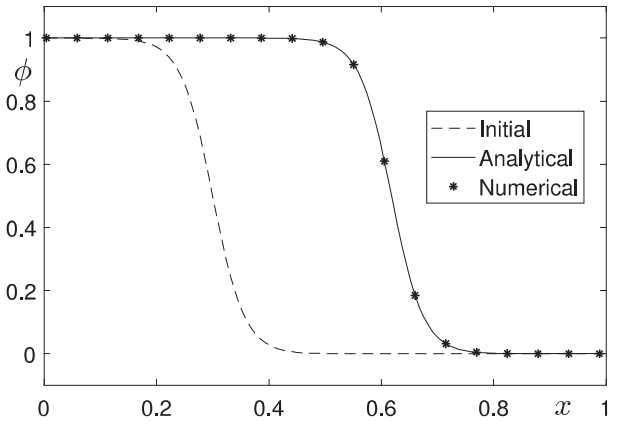

Fig. 9. Numerical traveling wave solution with an initial profile $\phi(x, y, 0) = 0.5(1 - \tanh((x - 0.3)/(2\sqrt{2}\epsilon)))$.

Table 1
l_2-norm error and temporal convergence rates with various Δt at $t = 0.004$.

Δt	1.0E-4	Rate	5.0E-5	Rate	2.5E-5
error	9.9364E-3	1.99	2.5098E-3	2.01	6.2318E-4

Table 2
l_2-norm error and temporal convergence rates with various h at $t = 0.0001$.

N_x	64	Rate	128	Rate	256
error	8.4875E-5	1.98	2.1569E-5	1.94	5.6025E-6

3.3. Convergence tests using traveling wave solutions

We perform convergence tests to validate the rate of convergence of the proposed algorithm using traveling wave solutions. When $\alpha = 2$, we have a traveling wave solution for the AC equation:

$$\phi(x, y, t) = 0.5\left(1 - \tanh\left(\frac{x - 0.3 - st}{2\sqrt{2}\epsilon}\right)\right), \tag{25}$$

where $s = 3/(\sqrt{2}\epsilon)$ is the speed of the traveling wave [36]. We take an initial condition on a domain $\Omega = (0, 1) \times (0, 1/8)$ as

$$\phi(x, y, 0) = 0.5\left(1 - \tanh\left(\frac{x - 0.3}{2\sqrt{2}\epsilon}\right)\right). \tag{26}$$

Fig. 9 shows the numerical and the analytical solutions at $t = 0.003$. The solutions are the slices at $y = h/2$. The parameter values used are $N_x = 128,\ N_y = N_x/8,\ h = 1/128,\ \Delta t = 1.0E - 5$, and $\epsilon = 0.02$.

The following tests verify that the proposed method is second-order accurate both in space and in time. First, we compute the discrete l_2-norm error with various temporal step sizes Δt and a fixed fine spatial step size h. We use the initial condition (26) and the parameters $N_x = 1024,\ N_y = N_x/8,\ h = 1/N_x,\ M_1 = M_2 = 501,\ \epsilon = 0.04$. Here, the final time is fixed to $t = 0.004$, the total number of time steps are used as $N_t = 40,\ 80,\ 160$, the temporal step size is defined as $\Delta t = T/N_t$, and $N_\tau = N_t/10$. We define the discrete l_2-norm error as follows:

$$\|e_{N_x}^{N_t}\|_2 = \sqrt{\frac{1}{N_x}\sum_{i=1}^{N_x}(\phi_{i,1}^{N_t} - \phi(x_i, y_1, N_t\Delta t))^2}.$$

The rate of convergence in time is defined as $\log_2(\|e_{N_x}^{N_t}\|_2/\|e_{N_x}^{2N_t}\|_2)$. Table 1 lists the l_2-norm error and temporal convergence rates.

Next, we demonstrate the discrete l_2-norm errors with various spatial step sizes h and a fixed fine temporal step size Δt. We use the same initial condition (26) and the parameters $\Delta t = 5.0E - 7,\ N_t = 200,\ M_1 = M_2 = 501,\ N_\tau = 16$, and $\epsilon = 0.02$. Here, $N_x = 64,\ 128,\ 256,\ N_y = N_x/8$, and $h = 1/N_x$, The rate of convergence in space is defined as $\log_2(\|e_{N_x}^{N_t}\|_2/\|e_{2N_x}^{N_t}\|_2)$. Table 2 lists the l_2-norm error and spatial convergence rates.

From these convergence tests, we can confirm the proposed scheme is indeed second-order accurate in time and space.

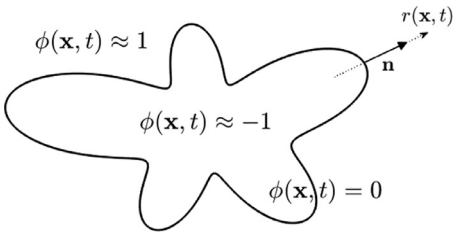

Fig. 10. Schematic illustration of the local coordinate $r(\mathbf{x},t)$.

3.4. Motion by mean curvature

In this section, we describe the intrinsic property, motion by mean curvature, of the AC equation with the high-order polynomial free energy. Let us consider the following signed distance of Cartesian coordinates $\mathbf{x}=(x,y)$ and $\mathbf{x}=(x,y,z)$ in the two- and three- dimensional space, respectively: $r(\mathbf{x},t)=\text{dist}(\mathbf{x},\Gamma)\text{sgn}(\phi(\mathbf{x},t))$, where $\Gamma=\{\mathbf{x}\mid\phi(\mathbf{x},t)=0\}$ is a zero-level set and $\text{sgn}(\cdot)$ is a sign function. Fig. 10 depicts the schematic illustration to the local coordinate $r(\mathbf{x},t)$.

The outward unit normal vector to the interface is denoted by $\mathbf{n}=\nabla\phi/|\nabla\phi|$, which implies identities $\mathbf{n}\cdot\mathbf{n}=1$ and $\mathbf{n}\cdot\mathbf{n}_r=0$, where $\mathbf{n}_r$ is the rate of change of $\mathbf{n}$ in the direction of local coordinate $r(\mathbf{x},t)$. Therefore, we can rewrite the diffusion term $\Delta\phi$ with the relation $\phi_r=-\mathbf{n}\cdot\nabla\phi$ as follows:

$$\begin{aligned}\Delta\phi &= \nabla\cdot\nabla\phi=\nabla\cdot(|\nabla\phi|\mathbf{n})=\nabla\cdot((\nabla\phi\cdot\mathbf{n})\mathbf{n})=\nabla\cdot(-\phi_r\mathbf{n})\\ &= -\nabla\phi_r\cdot\mathbf{n}-\phi_r\nabla\cdot\mathbf{n}=-(\nabla\phi)_r\cdot\mathbf{n}-\phi_r\nabla\cdot\mathbf{n}=(\phi_r\mathbf{n})_r\cdot\mathbf{n}-\phi_r\nabla\cdot\mathbf{n}\\ &= (\phi_{rr}\mathbf{n}+\phi_r\mathbf{n}_r)\cdot\mathbf{n}-\phi_r\nabla\cdot\mathbf{n}=\phi_{rr}-\phi_r\nabla\cdot\mathbf{n}.\end{aligned}$$

In two-dimensional space, the following equality holds because it holds that $\nabla\cdot\mathbf{n}=-\kappa$ with the principal curvatures κ, $\Delta\phi=\phi_{rr}+\kappa\phi_r$. Then, the kinetic equation as follows:

$$\phi_t=-\frac{F'(\phi)}{\epsilon^2}+\phi_{rr}+\kappa\phi_r. \tag{27}$$

The equation holds $-F'(\phi)/\epsilon^2+\phi_{rr}\approx 0$ for the planar interface at equilibrium. Then, Eq. (27) is rewritten as $\phi_t=\kappa\phi_r$ and we obtain the following equation $r_t=-\phi_t/\phi_r=-\kappa$. since the velocity of zero level-set $\Gamma_t=\{(x,y):\phi(x,y,t)=0\}$ is given as

$$0=\frac{d}{dt}\phi(r,t)\bigg|_{\Gamma_t}=\phi_r r_t+\phi_t.$$

Therefore, every interface between the two phases operates with the velocity V, which holds given as $V=-\kappa=-1/R$, where R is the principal radius of curvatures at the point of the surface. In this way, we can obtain a similar result in three-dimensional space. In three-dimensional space, because it holds that $\nabla\cdot\mathbf{n}=-(\kappa_1+\kappa_2)$ with the principal curvatures κ_1 and κ_2, a similar derivation results in $V=-(\kappa_1+\kappa_2)=-(1/R_1+1/R_2)$, where R_1 and R_2 are the principal radius of curvatures at the point of the surface. Please refer to [37] for more details.

Let R_0 be the initial radius of circle. The radius at time t is denoted as $R(t)$ and is defined by $R(t)=\sqrt{R_0^2-2t}$. In Fig. 11, the initial condition is defined as

$$\phi(x,y,0)=\tanh\left(\frac{R_0-\sqrt{x^2+y^2}}{\sqrt{2}\epsilon}\right) \tag{28}$$

on the computational domain $\Omega=(-1.2,1.2)\times(-1.2,1.2)$ with 256×256 mesh. Here, $R_0=1$, $h=2.4/256$, $\epsilon=0.05$, $\Delta t=1.0E-4$, and $\alpha=2,\ 4,\ 6,\ 8,\ 10$ are used.

Fig. 11 (a) shows the change of radius $R(t)$ due to the motion by mean curvature of the AC equation until $t=0.4$. The inscribed small figures are the zero-level contours corresponding times. Fig. 11(b) and (c) are the snapshots of ϕ with $\alpha=2$ and $\alpha=10$ at $t=0.2$, respectively. Fig. 11(d) shows the numerical transition width from -0.95 to 0.95 for $\alpha=2$ and $\alpha=10$ at $t=0.2$. From these results, we can observe that the AC equation with the high-order polynomial free energy has sharp interfacial transition layer.

Next, the evolution of a star-shaped interface with low- and high-order polynomial potentials are performed in the computational domain $\Omega=(-\pi,\ \pi)\times(-\pi,\ \pi)$, with mesh size $N_x=N_y=256$. Parameters are set as $h=2\pi/256$, $\Delta t=1.0E-4$, and $\epsilon=0.03$. The initial configuration is defined as

$$\phi(x,y,0)=\tanh\frac{2+0.6\cos(10\tan^{-1}(y/x))-\sqrt{x^2+y^2}}{\sqrt{2}\epsilon}. \tag{29}$$

Fig. 12 shows the results of temporal evolutions using the AC equation with the low- and high-order polynomial free energies with $\alpha=2$ and 10.

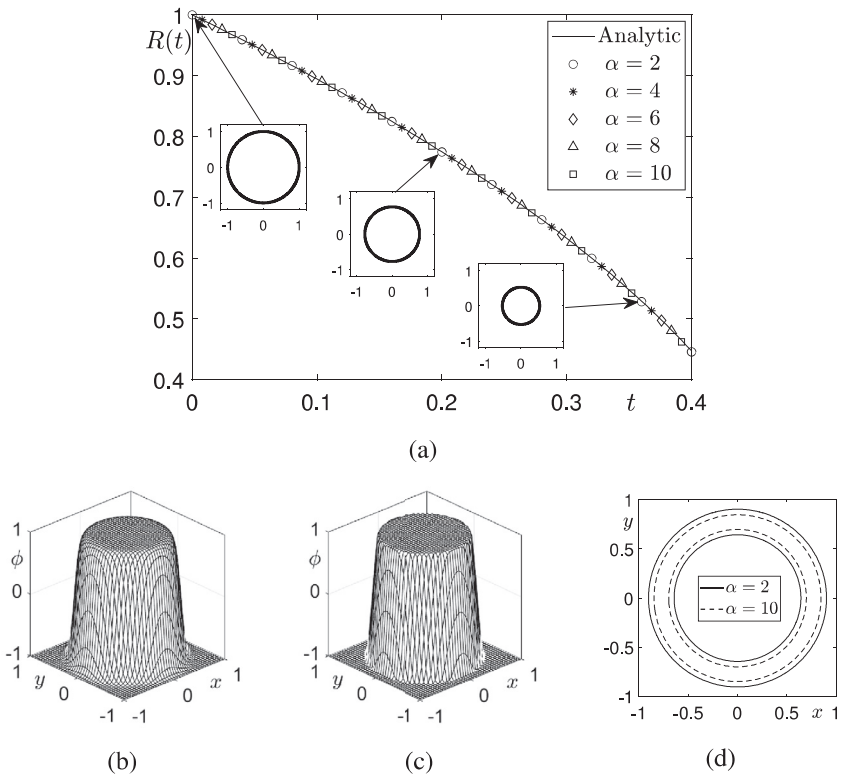

Fig. 11. (a) Change of radius $R(t)$ over time with the order $\alpha = 2,\ 4,\ 6,\ 8,$ and 10. (b)–(c) Snapshots of ϕ with $\alpha = 2$ and $\alpha = 10$ at $t = 0.2$, respectively. (d) Numerical transition width from -0.95 to 0.95 for $\alpha = 2$ and $\alpha = 10$ at $t = 0.2$.

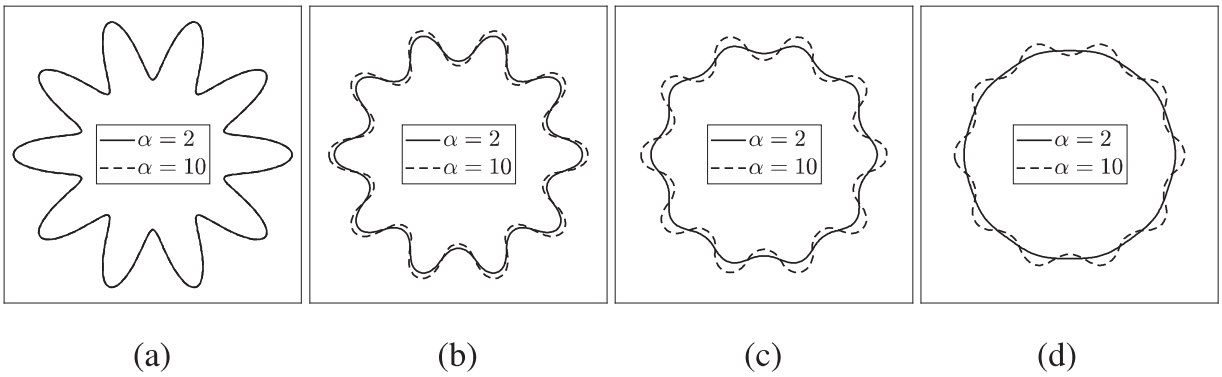

Fig. 12. Temporal evolution of the AC equation with star-shaped initial condition at (a) $t = 0$, (b) $t = 500\Delta t$, (c) $t = 1000\Delta t$, and (d) $t = 1800\Delta t$, respectively.

We then perform a sphere perturbed with a spherical harmonic mode to show the evolution with low- and high-order polynomial potentials in the computational domain $\Omega = (-1.2,\ 1.2) \times (-1.2,\ 1.2) \times (-1.2,\ 1.2)$, with mesh size $N_x = N_y = N_z = 64$. Parameters are set as $h = 2.4/64,\ \Delta t = 1.0E\ -\ 4$, and $\epsilon = 0.03$. The initial configuration is defined as

$$\phi(x, y, z, 0) = \tanh \frac{0.8 + 0.8 Y_{10,7}(\theta, \psi) - \sqrt{x^2 + y^2 + z^2}}{\sqrt{2}\epsilon}, \tag{30}$$

where $Y_{10,7}$ is a spherical harmonic [38],

$$\theta = \begin{cases} \tan^{-1} \frac{y}{x}, & \text{if } x \in (0, 32h), \\ \pi + \tan^{-1} \frac{y}{x}, & \text{otherwise.} \end{cases} \tag{31}$$

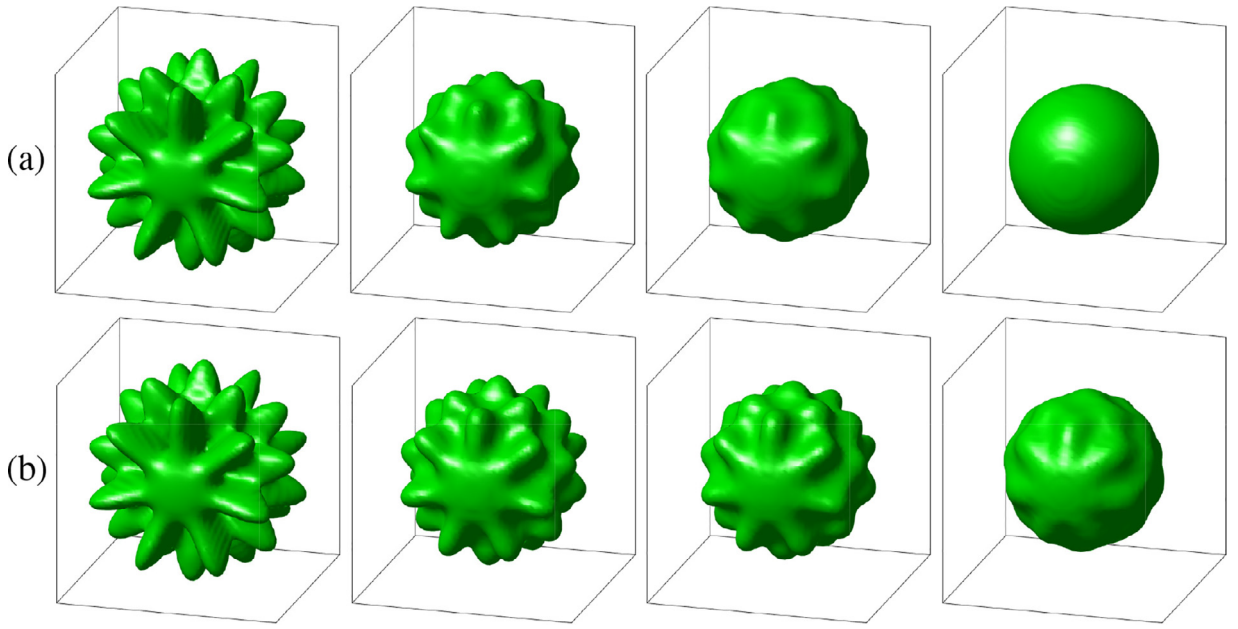

Fig. 13. Temporal evolution of the AC equation with 3*D* star-shaped initial condition. Here, (a) $\alpha = 2$ and (b) $\alpha = 10$ are used. From left to right, the evolutionary times at each column are $t = 0,\ 100\Delta t,\ 150\Delta t$, and $300\Delta t$, respectively.

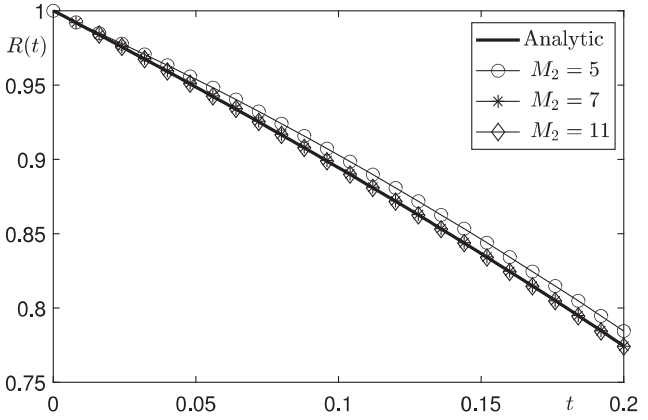

Fig. 14. Change of radius $R(t)$ over time with the order $\alpha = 6$ and various values of M_2.

is a polar angle, and $\psi = \cos^{-1}(z/\sqrt{x^2+y^2+z^2})$ is the azimuthal angle. Fig. 13(a) and (b) show the results of temporal evolutions at $t = 0,\ 100\Delta t,\ 150\Delta t$, and $300\Delta t$ using the AC equation with the low- and high-order polynomial free energy with $\alpha = 2$ and 10, respectively.

From left to right, the evolutionary times at each column are $t = 0,\ 50\Delta t,\ 100\Delta t$, and $500\Delta t$, respectively.

3.5. Effect of M_2 on the accuracy of the method

In this section, let us consider the effect of M_2 on the accuracy of the proposed method. We set the initial condition (28) on domain $\Omega = (-1.2, 1.2) \times (-1.2, 1.2)$ with $N_x = N_y = 128$. The parameters for this test are used as follows: $R_0 = 1$, $\alpha = 6$, $h = 2.4/128$, $\epsilon = 0.09$, $\Delta t = 2.0E-4$, and $N_\tau = 16$. When M_1 is fixed to 101, we use three values of M_2, i.e., $M_2 = 7,\ 11$, and 15. We compare the radii $R(t)$ of analytic and numerical solutions until the time $t = 0.2$. As shown in Fig. 14, a numerical solution is different from the analytic solution when a small value of M_2 are used. The result with $M_2 = 15$ is sufficiently accurate.

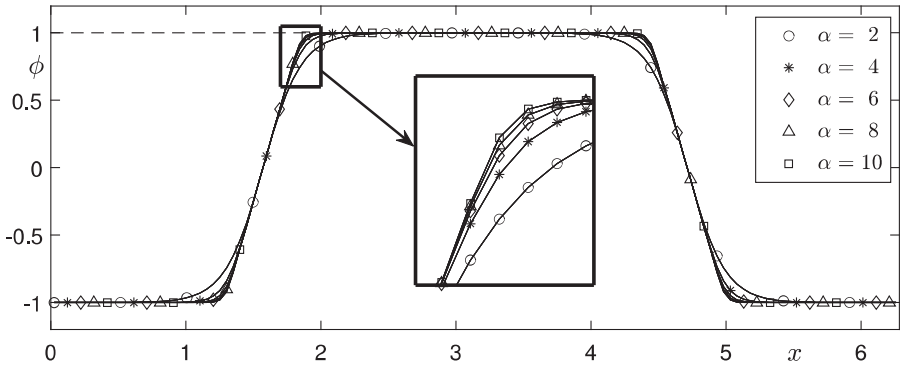

Fig. 15. Equilibrium states of $\phi(x, y, 0) = -\cos(x)$ for each $\alpha = 2,\ 4,\ 6,\ 8,$ and 10.

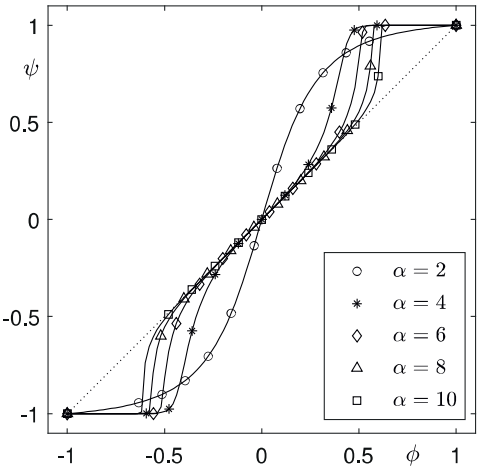

Fig. 16. At $t = 70\Delta t$, the numerical solutions of Eq. (32) with $\alpha = 2,\ 4,\ 6,\ 8,$ and 10.

3.6. Equilibrium interfacial transition profiles

To see the effect of different α on the equilibrium interfacial transition profiles, we perform the numerical experiment on the computational domain $\Omega = (0, 2\pi) \times (0, \pi/16)$ with $N_x = 128$ and $N_y = 4$ using the initial condition, $\phi(x, y, 0) = -\cos(x)$. In this test, the parameters are set to be $h = 2\pi/128$, $\epsilon = 0.2$, and $\Delta t = 1.0E-4$. We use five different α values, i.e., $\alpha = 2,\ 4,\ 6,\ 8,$ and 10. Fig. 15 shows the equilibrium states at $t = 3000\Delta t$ with various values of α. As the value of α increases, the interfacial transition layer becomes sharper.

3.7. Effect of α on the dynamics of the AC equation

Let us consider the nonlinear term in Eq. (1):

$$\frac{\partial \psi(t)}{\partial t} = -\frac{F'_\alpha(\psi(t))}{\epsilon^2}, \quad t > 0. \tag{32}$$

Fig. 16 shows the numerical solutions at $t = 100\Delta t$ of Eq. (32) for $\alpha = 2,\ 4,\ 6,\ 8,$ and 10 with $h = 2.4/128$ and $\epsilon = 0.075$. Here, for simplicity, we use the explicit Euler's method with $\Delta t = 1.0E-4$ and $S_t = 4$:

$$\psi^{k+1} = \psi^k - \Delta t \frac{F'_\alpha(\psi^k)}{\epsilon^2}, \tag{33}$$

where the initial condition is $\psi^0 = \phi$. As the value of α increases, the evolution of the value of ψ is faster in the region $|\phi| \approx 0$ and slower in the region $|\phi| \approx 1$.

To see this effect clearly, we perform the numerical experiment using the initial condition $\phi(x, y, 0) = -0.3\cos(x)$ in domain $\Omega = (0, 2\pi) \times (0, \pi/16)$ with 128×4. Here, we use $h = 2\pi/128$, $\Delta t = 1.0E-4$, and $\epsilon = 0.2$ for parameters. Fig. 17 shows the snapshots of the numerical solutions of the AC equation with the various values of α at $t = 2000\Delta t$. As we expected, the evolutions with large values of α is slower than those with small values of α.

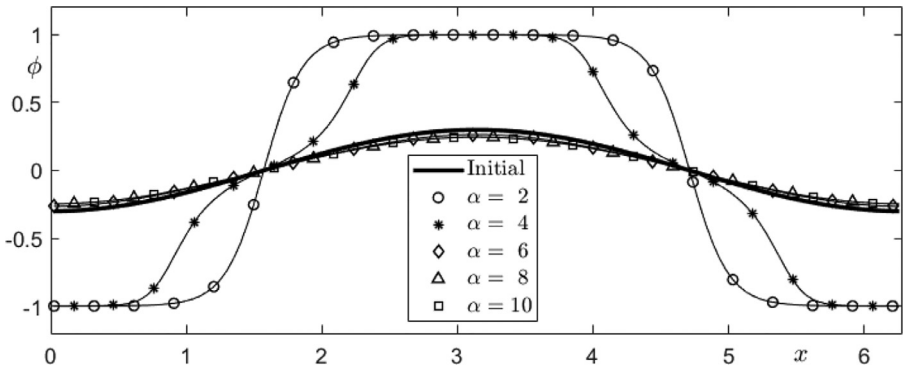

Fig. 17. Snapshots of the numerical solutions of the AC equation with the initial condition $\phi(x, y, 0) = -0.3\cos(x)$. Here, $t = 2000\Delta t$ and $\alpha = 2,\ 4,\ 6,\ 8,$ and 10.

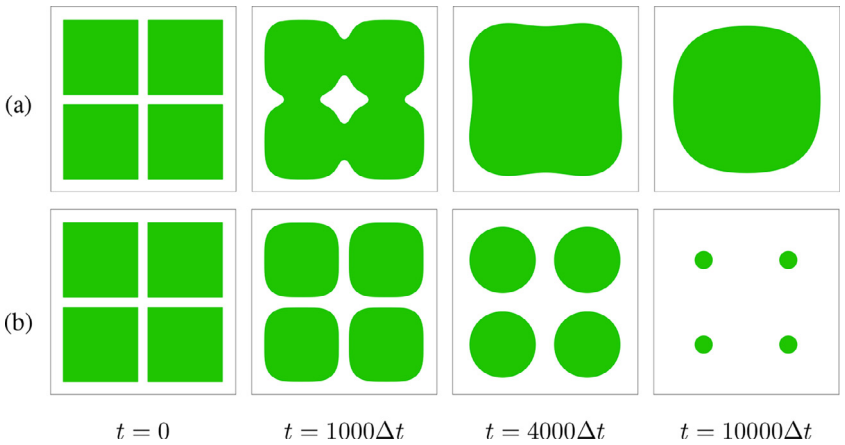

Fig. 18. Temporal evolutions of zero-contour lines of ϕ with (a) $\alpha = 2$ and (b) $\alpha = 10$. The times are given below each column.

Next, we present the effect of orders on the evolution of initially separated four squares on $\Omega = (0, 2\pi) \times (0, 2\pi)$. Here, we use $N_x = N_y = 256,\ h = 2\pi/256,\ \epsilon = 0.07,\ \Delta t = 1.0E - 4,$ and the final time $t = 1$. The following initial condition is employed:

$$\phi(x, y, 0) = \begin{cases} 1 & \text{if } x \in (17h, 122h) \cup (134h, 239h), \\ & \quad y \in (17h, 122h) \cup (134h, 239h), \\ -1 & \text{otherwise.} \end{cases} \tag{34}$$

Fig. 18(a) shows the temporal evolution of zero-contour lines of ϕ with $\alpha = 2$ and we can observe that the initially separated four squares merged and became one closed curve. However, in the case of $\alpha = 10,$ the four squares shrank without merging, see Fig. 18(b).

Another example is a spiral on $\Omega = (-1.2, 1.2) \times (-1.2, 1.2),$ see the first column in Fig. 19. The width of the spiral is $14h$. We define an initial value of ϕ as $\phi(x, y, 0) = 1$ in the inside of spiral and otherwise $\phi(x, y, 0) = -1$. Here, $N_x = N_y = 128,\ h = 2.4/128,\ \Delta t = 1.0E - 5,$ and $\epsilon = h$ are used. In Fig. 19(a) and (b), the results of temporal evolutions using the AC equation with the low-order polynomial free energies ($\alpha = 2,\ 4$) show the merging of interface, while using high-order free energy ($\alpha = 6$) maintains the interface as shown in Fig. 19(c).

We perform a similar test in the three-dimensional space. The initial condition is shown in the first column in Fig. 20. The height of the three-dimensional spiral on $\Omega = (-1.2, 1.2) \times (-1.2, 1.2) \times (-1.2, 1.2)$ is $58h$ and the width is $8h$. The parameters used are $N_x = N_y = N_z = 64,\ h = 2.4/64,\ \Delta t = 1.0E - 4,$ and $\epsilon = h$. An initial value of ϕ is defined as $\phi(x, y, z, 0) = 1$ in the inside of the spiral and otherwise $\phi(x, y, z, 0) = -1$. In Fig. 20(a) and (b), the results of temporal evolutions using the AC equation with the low-order polynomial free energy ($\alpha = 2,\ 4$) show the merging of interface, while using high-order free energy ($\alpha = 6$) maintains the interface as shown in Fig. 19(c).

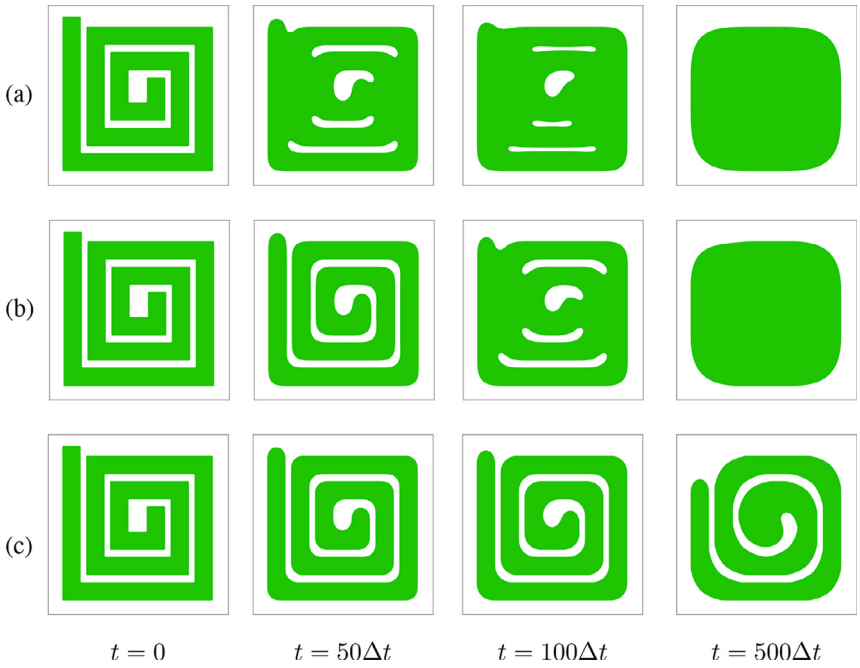

Fig. 19. Temporal evolution of the AC equation with square spiral shape initial condition. Here, (a) $\alpha = 2$, (b) $\alpha = 4$ and (c) $\alpha = 6$ are used. From left to right, the evolutionary times at each column are $t = 0$, $50\Delta t$, $100\Delta t$, and $500\Delta t$, respectively.

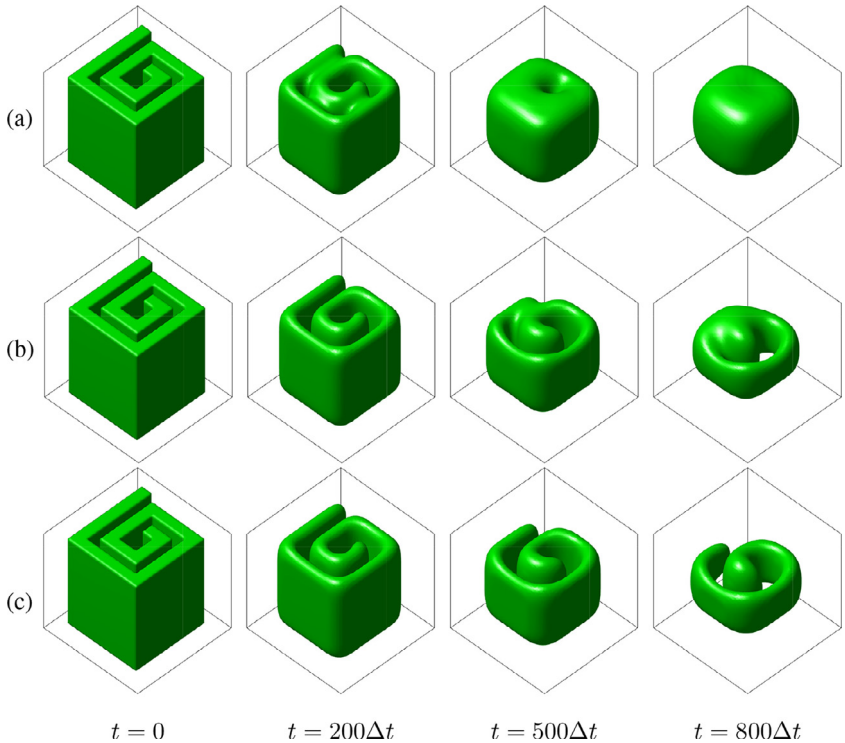

Fig. 20. Temporal evolution of the AC equation with three-dimensional square spiral shape initial condition. Here, (a) $\alpha = 2$, (b) $\alpha = 4$ and (c) $\alpha = 6$ are used. From left to right, the evolutionary times at each column are $t = 0$, $200\Delta t$, $500\Delta t$, and $800\Delta t$, respectively.

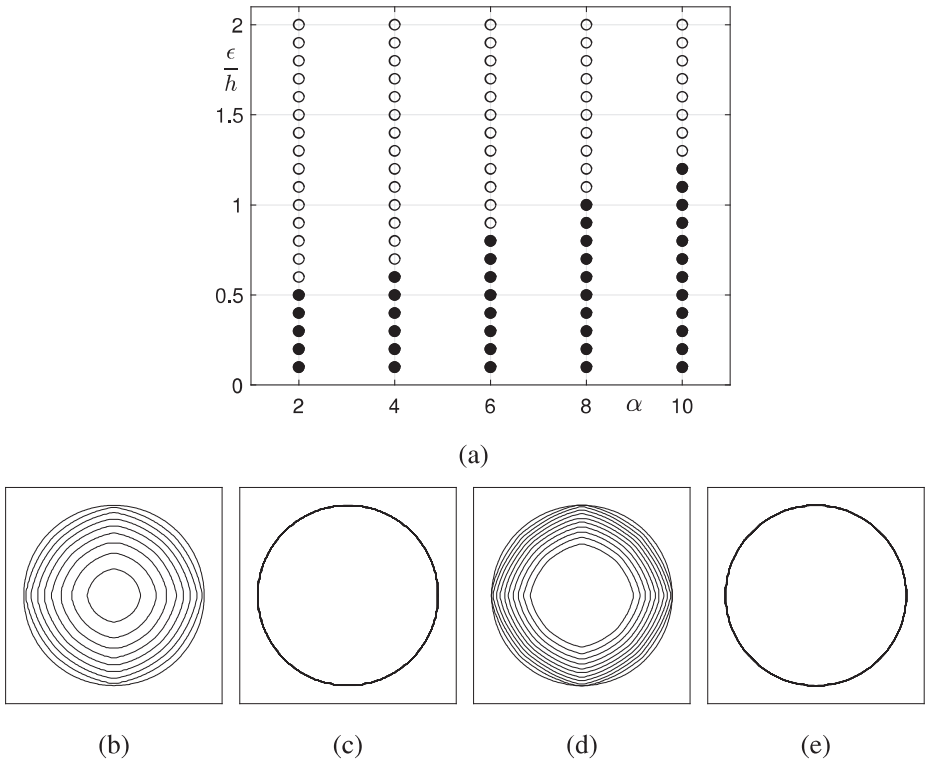

Fig. 21. (a) Evolution intervals (white circles) and pinning intervals (black circles). (b)–(e) Until $t = 10000\Delta t$, temporal evolutions of numerical solution of the AC equation with $\alpha = 2$ for (b) $\epsilon = 0.6h$, (c) $\epsilon = 0.5h$, and of the AC equation with $\alpha = 4$ for (d) $\epsilon = 0.7h$, (e) $\epsilon = 0.6h$.

3.8. Effect of ϵ on the pinning phenomenon

Finally, we study the pinning interval depending on the value of ϵ on $\Omega = (-1.2,\ 1.2) \times (-1.2,\ 1.2)$. Here, the initial condition is used as

$$\phi(x, y, 0) = \tanh\left(\frac{1 - \sqrt{x^2 + y^2}}{\sqrt{2}\epsilon}\right). \tag{35}$$

The parameters are used as $N_x = N_y = 128$, $h = 2.4/128$, and $\Delta t = 1.0E - 4$. For each polynomial free energy order α, the black circles represent the intervals of ϵ value which make the interface be pinned. On the other hand, the white circles represent evolution intervals. To illustrate the pinning phenomenon, we perform the numerical simulation of the AC equation with $\alpha = 2$ (Fig. 21(b) and (c)) and $\alpha = 4$ (Fig. 21(d) and (e)) until $t = 10000\Delta t$. As shown in Fig. 21(b) and (d), we can observe that the initial circle shrinks using $\epsilon = 0.6h$ and $\epsilon = 0.7h$, respectively. Meanwhile, we can observe that the initial circle is pinned using $\epsilon = 0.5h$ and $\epsilon = 0.6h$, in Fig. 21(c) and (e), respectively.

4. Conclusions

In this study, we proposed an unconditionally stable numerical method for the AC equation with high-order (higher than fourth) polynomial free energy. High-order (greater than fourth) polynomial free energy potentials can be used in the total energy functional and can better represent interfacial dynamics of the AC equation. However, the AC equation with the high-order polynomial is getting stiffer as the polynomial order increases. To resolve this problem, we proposed an interpolation method. First, we solve the nonlinear double-well potential term using interpolation from the pre-computed values. Second, we solve the diffusion equation using the Crank–Nicolson method and multigrid method. The overall scheme is unconditionally stable and we theoretically proved the unconditional stability. Various computational experiments were performed to demonstrate the accuracy and the robustness of the proposed method and we highlighted the different dynamics for the AC equation with polynomial free energy of various orders. The numerical results confirmed that the proposed method would be useful for modeling various interfacial phenomena. As future research, we will apply the developed scheme to incompressible multiphase fluid flow modeling and simulation. We will also investigate the unconditionally energy stable numerical schemes for the AC equation with high-order polynomial free energy.

Declaration of Competing Interest

The authors declare that they have no known competing financial interests or personal relationships that could have appeared to influence the work reported in this paper.

CRediT authorship contribution statement

Chaeyoung Lee: Methodology, Software, Validation, Investigation, Writing - original draft, Writing - review & editing, Visualization, Funding acquisition. **Hyundong Kim:** Validation, Investigation, Writing - original draft, Writing - review & editing, Visualization, Funding acquisition. **Sungha Yoon:** Validation, Investigation, Writing - original draft, Writing - review & editing, Visualization. **Sangkwon Kim:** Validation, Investigation, Writing - original draft, Writing - review & editing, Visualization. **Dongsun Lee:** Validation, Formal analysis, Investigation, Writing - original draft, Writing - review & editing. **Jinate Park:** Validation, Investigation, Writing - original draft, Writing - review & editing, Visualization. **Soobin Kwak:** Validation, Investigation, Writing - original draft. **Junxiang Yang:** Software, Resources, Writing - original draft. **Jian Wang:** Validation, Writing - original draft. **Junseok Kim:** Conceptualization, Methodology, Software, Validation, Investigation, Writing - original draft, Writing - review & editing, Supervision, Project administration, Funding acquisition.

Acknowledgments

The first author (C. Lee) was supported by Basic Science Research Program through the National Research Foundation of Korea(NRF) funded by the Ministry of Education (NRF-2019R1A6A3A13094308). H. Kim was supported by Basic Science Research Program through the National Research Foundation of Korea(NRF) funded by the Ministry of Education (NRF-2020R1A6A3A13077105). The corresponding author (J.S. Kim) was supported by Basic Science Research Program through the National Research Foundation of Korea(NRF) funded by the Ministry of Education(NRF-2019R1A2C1003053). The authors would like to thank the reviewers for their constructive and helpful comments on the revision of this article.

References

[1] Allen SM, Cahn JW. A microscopic theory for antiphase boundary motion and its application to antiphase domain coarsening. Acta Metall 1979;27:1085–95.
[2] Benes M, Chalupecky V, Mikula K. Geometrical image segmentation by the Allen–Cahn equation. Appl Numer Math 2004;51:187–205.
[3] Takaki T, Shimokawabe T, Ohno M, Yamanaka A, Aoki T. Unexpected selection of growing dendrites by very-large-scale phase-field simulation. J Cryst Growth 2013;382:21–5.
[4] Zhao J, Wang Q, Yang X. Numerical approximations for a phase field dendritic crystal growth model based on the invariant energy quadratization approach. Int J Numer Methods Eng 2017;110:279–300.
[5] Feng X, Li Y. Analysis of symmetric interior penalty discontinuous Galerkin methods for the Allen–Cahn equation and the mean curvature flow. IMA J Numer Anal 2015;35:1622–51.
[6] Ronsin O.J., Jang D., Egelhaaf H.J., Brabec C.J., Harting J.. A phase-field model for the evaporation of thin film mixtures. 2020. arXiv:2001.05160.
[7] Ren F, Song B, Sukop MC, Hu H. Improved lattice Boltzmann modeling of binary flow based on the conservative Allen–Cahn equation. Phys Rev E 2016;94:023311.
[8] Rizwan M, Shah A, Yuan L. A central compact scheme for numerical solution of two-phase incompressible flow using Allen–Cahn phase field model. J Braz Soc Mech Sci Eng 2016;38:433–41.
[9] Ma L, Chen R, Yang X, Zhang H. Numerical approximations for Allen–Cahn type phase field model of two-phase incompressible fluids with moving contact lines. Commun Comput Phys 2017;21:867–89.
[10] Kim J, Lee S, Choi Y. A conservative Allen–Cahn equation with a space-time dependent lagrange multiplier. Int J Eng Sci 2014;84:11–17.
[11] Lee D, Kim Y. Novel mass-conserving Allen–Cahn equation for the boundedness of an order parameter. Commun Nonlinear Sci Numer Simul 2020;85:105224.
[12] Lee HG, Yang J, Kim J. Pinning boundary conditions for phase-field models. Commun Nonlinear Sci Numer Simul 2020;82:105060.
[13] Shah A, Sabir M, Qasim M, Bastian P. Efficient numerical scheme for solving the Allen–Cahn equation. Numer Methods Partial Differ Equ 2018;34(5):1820–33.
[14] Li C, Huang Y, Yi N. An unconditionally energy stable second order finite element method for solving the Allen–Cahn equation. J Comput Appl Math 2019;353:38–48.
[15] Shen J, Tang T, Yang J. On the maximum principle preserving schemes for the generalized Allen–Cahn equation. Commun Math Sci 2016;14(6):1517–34.
[16] He D, Pan K. Maximum norm error analysis of an unconditionally stable semi-implicit scheme for multi-dimensional Allen–Cahn equations. Numer Methods Partial Differ Equ 2019;35(3):955–75.
[17] Ayub S, Affan H, Shah A. Comparison of operator splitting schemes for the numerical solution of the Allen–Cahn equation. AIP Adv 2019;9(12):125202.
[18] Weng Z, Tang L. Analysis of the operator splitting scheme for the Allen–Cahn equation. Numer Heat Transf B-Fund 2016;70(5):472–83.
[19] Hou T, Xiu D, Jiang W. A new second-order maximum-principle preserving finite difference scheme for Allen–Cahn equations with periodic boundary conditions. Appl Math Lett 2020;104:106265.
[20] Ji B, Liao HL, Gong Y, Zhang L. Adaptive linear second-order energy stable schemes for time-fractional Allen–Cahn equation with volume constraint. Commun Nonlinear Sci Numer Simul 2020:105366.
[21] Yan Y, Chen W, Wang C, Wise SM. A second-order energy stable BDF numerical scheme for the Cahn–Hilliard equation. Commun Comput Phys 2018;23(2):572–602.
[22] Cheng K, Feng W, Wang C, Wise SM. An energy stable fourth order finite difference scheme for the Cahn–Hilliard equation. J Comput Appl Math 2019;362:574–95.
[23] Wu X, Van Zwieten GJ, Van der Zee KG. Stabilized second-order convex splitting schemes for Cahn–Hilliard models with application to diffuse-interface tumor-growth models. Int J Numer Method Biomed Eng 2014;30(2):180–203.
[24] Cheng K, Wang C, Wise SM, Yue X. A second-order, weakly energy-stable pseudo-spectral scheme for the Cahn–Hilliard equation and its solution by the homogeneous linear iteration method. J Sci Comput 2016;69(3):1083–114.
[25] Chen W, Wang C, Wang S, Wang X, Wise SM. Energy stable numerical schemes for ternary Cahn–Hilliard system. J Sci Comput 2020;84:27.
[26] Tsou NT, Huber JE, Shu YC. A sharp interface model of compatible twin patterns in shape memory alloys. Smart Mater Struct 2012;21(9):094010.
[27] Shin J, Yang J, Lee C, Kim J. The Navier–Stokes–Cahn–Hilliard model with a high-order polynomial free energy. Acta Mech 2020;231:2425–37.

[28] Lee HG, Yang J, Park J, Kim J. Effect of space dimensions on equilibrium solutions of Cahn–Hilliard and conservative Allen–Cahn equations. Numer Math Theor Meth Appl 2020;13(3):644–64.
[29] Lee HG. A semi-analytical fourier spectral method for the Swift–Hohenberg equation. Comput Math Appl 2017;74(8):1885–96.
[30] Chertock A, Kurganov A, Petrova G. Fast explicit operator splitting method for convection-diffusion equations. Int J Numer Methods Fluids 2009;59(3):309–32.
[31] Holden H, Karlsen K, Risebro N, Tao T. Operator splitting for the KdV equation. Math Comput 2011;80(274):821–46.
[32] Hu L, Feng S. A robust and contact preserving flux splitting scheme for compressible flows. Commun Nonlinear Sci Numer Simul 2021;93:105502.
[33] Li Y, Lee HG, Jeong D, Kim J. An unconditionally stable hybrid numerical method for solving the Allen–Cahn equation. Comput Math Appl 2010;60(6):1591–606.
[34] Thomas JW. Numerical partial differential equations: finite difference methods, Vol 22. Berlin: Springer; 2013.
[35] Trottenberg U, Schüller A, Oosterlee CW. Multigrid methods. London: Academic Press; 2000.
[36] Wazwaz AM. The tanh–coth method for solitons and kink solutions for nonlinear parabolic equations. Appl Math Comput 2007;188(2):1467–75.
[37] Lee D, Kim J. Mean curvature flow by the Allen–Cahn equation. Eur J Appl Math 2015;26:535–59.
[38] Cristini V, Lowengrub J. Three-dimensional crystal growth–II: nonlinear simulation and control of the Mullins–Sekerka instability. J Cryst Growth 2004;266:552–67.